

Source characterization of full-scale jet noise using acoustic intensity

Trevor A. Stout^{a)}, Kent L. Gee^{b)}, Tracianne B. Neilsen^{c)}, Alan T. Wall^{d)} and Michael M. James^{e)}

(Received: 5 August 2015; Revised: 16 November 2015; Accepted: 16 November 2015)

Vector acoustic intensity provides both the direction and magnitude of energy flow at the probe location and is, hence, more informative than acoustic pressure measurements. However, this important quantity has seen little application previously in aeroacoustics. In the present work, an intensity probe, consisting of four microphones, captured the radiated field to the sideline and aft of a tethered, full-scale military jet aircraft as one engine was operated at multiple engine conditions. Data from each probe location provide a frequency-dependent map of the sound flow near the aircraft. The vector acoustic intensity is estimated using a recently developed processing technique that extends the upper-frequency limit of the traditional cross-spectrum-based calculations. The dominant intensity vectors are traced back to the jet centerline as a method of approximating the extent and location of the source region as a function of frequency. As expected for jet mixing noise sources, the resulting source region estimates contract and move upstream with increasing frequency. A comparison of estimated source regions and intensity directionalities between military and afterburner engine conditions reveals important distinctions in the sound fields. © 2015 Institute of Noise Control Engineering.

Primary subject classification: 13.1.5; Secondary subject classification: 72.3

1 INTRODUCTION

Vector acoustic intensity measurements, which can characterize the flow of sound energy around and from a radiating source, are an important tool within acoustical engineering and noise control. Because the active intensity normal to a measurement surface is the acoustic power flux, standardized methods^{1–3} for obtaining sound power from intensity measurements have been developed. In addition to obtaining radiated power, intensity has been used in other applications, including sound emission from noise sources in situ⁴, noise source identification^{5,6}, building insulation^{7,8} and characterizing the

transmission loss⁹ and radiation from vibrating plates and panels. Intensity measurements have been used as a near-field sensing strategy in active noise control¹⁰ and in sound field reconstruction¹¹ and pressure/particle velocity measurements have been used to improve near-field acoustical holography methods^{12,13}.

Despite the growth of intensity measurements into a robust engineering tool over the past few decades, the technique has had little previous application in jet aeroacoustics. Studies of the sound field near a turbulent jet flow typically involve arrays of microphones outside of the jet plume^{14–18}, yet these arrays are usually not chosen or optimized for vector acoustic intensity estimation. As noted by Greska¹⁹, the vector nature of this quantity has been previously neglected, as it has often been effectively equated with squared pressure. Until recently, there have been two examples of the use of vector acoustic intensity measurements in jet noise analysis. First, the most in-depth example of analyzing intensity from jet noise sources were two-dimensional intensity measurements by Jaeger and Allen²⁰ of a Mach 0.2–0.6 laboratory-scale, unheated jet. Jaeger and Allen traced intensity vectors directly back to the jet centerline, using the intercepts to describe the source region. Second, although some details about the experiment are not given, Ventakesh et al.²¹ used a one-dimensional sound intensity probe in the near-field to verify source

^{a)} Department of Physics and Astronomy, Brigham Young University, Provo, UT 84602, USA; email: trevor.stout@hotmail.com.

^{b)} Department of Physics and Astronomy, Brigham Young University, Provo, UT 84602, USA; email: kentgee@physics.byu.edu.

^{c)} Department of Physics and Astronomy, Brigham Young University, Provo, UT 84602, USA; email: tbn@byu.edu.

^{d)} Air Force Research Laboratory, Wright-Patterson Air Force Base, OH 45433, USA; email: alan.wall.2.ctr@us.af.mil.

^{e)} Blue Ridge Research and Consulting, LLC, 29 N Market St., Suite 700, Asheville, NC 28801, USA; email: michael.james@blueridgeresearch.com.

distributions for a high-subsonic, heated jet flow, obtained via a new beamforming approach. As expected from the low Mach numbers in both experiments, the intensity vectors were found to originate from a relatively compact region.

This paper contains analysis of the vector intensity field near an installed, high-powered military jet engine, in an effort to better understand the acoustic source and radiation characteristics and to demonstrate the utility of intensity in jet aeroacoustic analysis. Full-scale tactical engine and aircraft measurements^{22–27} are relatively rare for various logistical reasons and near-field measurements are further complicated by the high sound levels. The measurements described here were carried out during the development of a sound intensity measurement capability for rocket noise source characterization, which represents an even harsher measurement environment than that near a military jet engine. The robustness of the same intensity probe was shown in measurements of the sound field near horizontally-fired solid rocket motors^{28,29} and preliminary, limited analyses of the intensity data further explored here have been reported in Refs. 30 and 31. In these analyses, acoustic intensity vectors indicate an extended source region in the jet, consistent with other studies of full-scale turbulent flows^{25,32}.

In this paper, the experimental setup is first described, with an emphasis on the four-microphone intensity probe configuration used. Implementation of a recently developed intensity calculation method³³, which allows for more accurate intensity estimation over a much broader frequency range when compared with traditional methods, is described. Resultant intensity maps at afterburner and military (full-throttle) engine conditions are displayed at several one-third octave band center frequencies. For each frequency, the maximum amplitude intensity region within the measurement aperture is defined to consist of locations at which the sound intensity level is within 3 dB of the maximum value. The angles of the intensity vectors contained within are evaluated to gain a better understanding of how the resultant maximum radiation direction compares to far-field directivity. Additionally, the intensity vectors from the 3 dB-down region are traced back to the jet centerline to provide an estimate of location and extent of the maximum source region. An evaluation of the meaning of this ray-tracing method is better understood through an analytical example involving the measurement geometry and a wavepacket-like source model. The source characterization results are analyzed as a function of frequency and engine condition (military and afterburner powers) to highlight the ability of the vector intensity in capturing the changes in the noise sources.

1.1 Experimental Setup

The acoustical data presented herein was taken by a team of researchers from Blue Ridge Research and Consulting, LLC and Brigham Young University in the vicinity of a tethered Lockheed Martin/Boeing F-22A Raptor (see Fig. 1) with one engine operated at multiple conditions while keeping the other engine idle. The primary purpose for these measurements was to perform near-field acoustical holography (NAH) using a point-to-point scan-based approach with a 90 microphone rectangular array [see Fig. 2(a)] and a stationary 50 microphone ground-based reference array. The experimental setup and data acquisition system developed for this purpose are described in Ref. 34. At afterburner and military engine conditions, data was taken at a sampling rate of 48 and 96 kHz, respectively. A significantly better understanding of the turbulent mixing noise in the geometric near field of a high-power military jet aircraft has resulted from the previous analysis of the data, using holography³⁵ and partial coherence decomposition³⁶, correlation and coherence analysis³⁷, multiple beamforming methods³⁸, similarity spectra analysis³⁹ and equivalent source modeling⁴⁰. Attached to the top of the 90 microphone array was a custom three-dimensional intensity probe [see Fig. 2(b) and Sec. 1.2] that was concurrently being developed for rocket noise source measurements. The probe was used to take measurements as the rectangular array was moved to different scan positions (see Fig. 3 and the intensity maps in Sec. 3) along two measurement planes, parallel to the estimated shear layer at offset distances of 4.1 m (measurement plane 1) and 5.6 m away (plane 2), as well as on an arc with radius 22.9 m (75 ft).

Because the results of this paper stem from the point-to-point measurements of the intensity vector field made with a single probe over many engine runups,



Fig. 1—Measurement setup, with F-22 tethered to concrete run-up pad. The rectangular microphone rig is visible on the right, atop an aluminum guide rail.

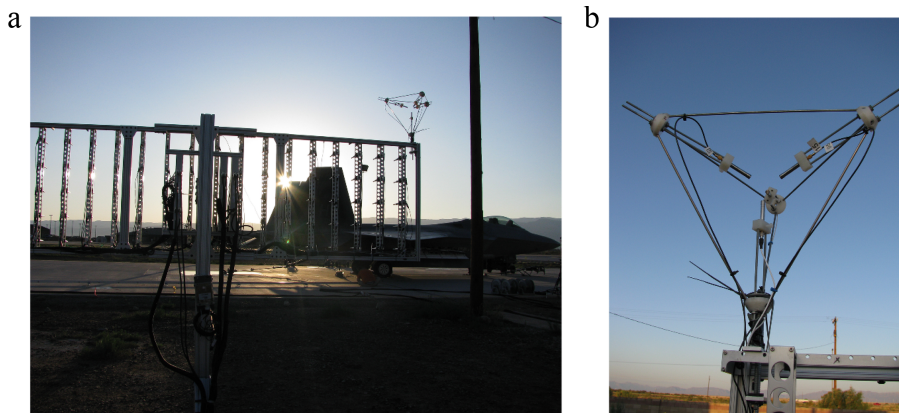


Fig. 2—View of 90-microphone rig with attached tetrahedral intensity probe (a) and close-up of intensity probe (b). The microphones are attached to the vertices of the tetrahedron, with diaphragms facing inward.

repeatability is crucial. The consistency of the measurements has been previously documented by analyses of the overall and spectral levels using the stationary, ground-based microphone array. For military and afterburner engine conditions, respectively, the standard deviation of the OASPLs across all scans averaged to <1 dB³⁴. Thus, the intensity measurements at each point can be combined to provide a single map of the intensity field near the F-22, within this error.

1.2 Tetrahedral Intensity Probe

This tetrahedral intensity probe design was developed for the rocket motor studies described in

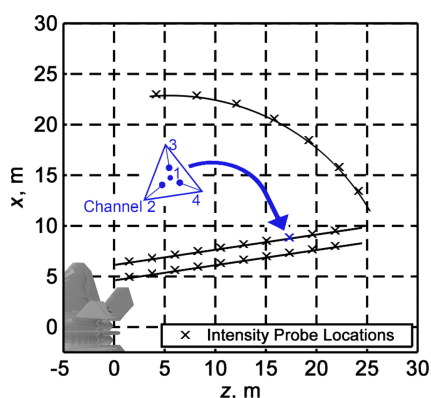


Fig. 3—Top-down schematic of intensity probe data locations along the measurement planes and arc (black). A rendering of the F-22 is partially visible near the origin, with the engine nozzle shown at the origin. Superimposed in blue, a schematic of the probe microphone orientation indicates channel number and placement. Compare with Fig. 2(b).

Refs. 28 and 29 [see Fig. 2(b)]. The external frame held four low-sensitivity GRAS 40BD prepolarized microphones with 26CB preamplifiers at the tetrahedron vertices, facing inward. The microphone diaphragms were positioned such that they could be circumscribed by a 3.81 cm diameter sphere. Laboratory testing of this probe configuration in anechoic conditions up to 2 kHz showed <1 dB maximum error in magnitude and $<10^\circ$ direction error⁴¹. The intensity probe was placed at a height of approximately 2.54 m for the subset of the data presented in this paper. Figure 3 displays the orientation of the probe microphones.

To illustrate the functionality of the intensity probe, examples of recorded waveforms on all four microphones are shown in Fig. 4, for two different measurement locations. Differences in the signal's apparent time of arrival at each microphone are visible, especially at the pressure increases that occur just before 1 ms in the time records. Near $z = 8$ m downstream, channel 4 received information well before channel 3, but this order is reversed near $z = 17$ m downstream. This ordering makes intuitive sense in light of the probe orientation detailed in Fig. 3 and assuming a peak source location near 5–6 m downstream. In the time domain, time of arrival analysis can estimate the apparent direction of signal propagation, or the overall intensity vector direction, not unlike beamforming³⁸ or phase speed characterizations³⁷. In the frequency domain, this time of arrival difference presents itself as differences in the complex pressures themselves, resulting in a non-zero imaginary part of the cross spectrum between microphone pairs. Traditional intensity estimation analysis finds that the imaginary part of the cross spectrum is directly proportional to the magnitude of the intensity component collinear with each microphone pair. In addition, time-of-arrival information is found in the phase of the transfer function between microphone pairs. The

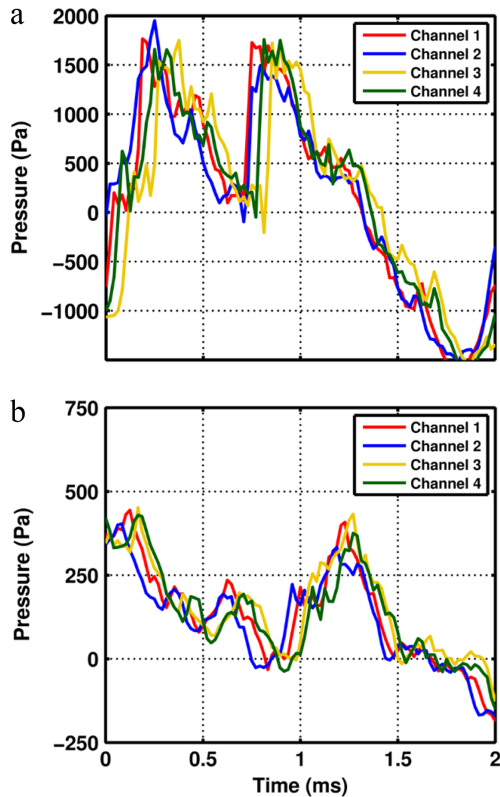


Fig. 4—Waveforms as recorded by the four intensity probe microphones at two different locations, (a) near $z = 8$ m and (b) near $z = 17$ m downstream. Note the apparent arrival time at each microphone differs between the two locations.

transfer functions between all four microphones may then be used (instead of the cross spectrum) to estimate the vector acoustic intensity as a function of frequency according to a new intensity estimation technique (see Sec. 2.1).

2 INTENSITY METHODOLOGY

The time-averaged acoustic vector intensity at a single point is obtained from the time-integrated product of the collocated acoustic particle velocity, a vector, and pressure, a scalar. The acoustic particle velocity, which is the more challenging to obtain, can be measured directly using, e.g., commercially available, specialized sensors involving a pair of heated wires⁴². However, these sensors are sensitive to nonacoustic velocity fluctuations, such as wind or entrained flow, which exist around a rocket or jet aircraft plume. The acoustic particle velocity can instead be approximated via the pressure gradient in Euler's equation using a multi-microphone probe that simultaneously gives the pressure using the same microphones. This approach is commonly used

and has been successfully applied to the near-field characterization of solid rocket motor plumes^{28,29,41}. The traditional calculation scheme for acoustic intensity is the finite difference (FD), or p-p method^{43,44}, which estimates the active component of the intensity between two microphones, approximating the particle velocity through a pressure spatial gradient. This estimation method suffers from frequency-dependent bias, underestimating the intensity magnitude and yielding errors in the direction as frequency increases^{43,44}, even when well below the spatial Nyquist limit. However, the phase and amplitude gradient estimator (PAGE)³³ method yields more accurate intensity estimates over a broader frequency range. Applied to the F-22 intensity estimations, the PAGE method extends the useable frequency limit from about 2 kHz to roughly 6 kHz. The PAGE method is used to produce the vector maps below (excepting Fig. 5, which is included to demonstrate the advantages of the PAGE method). Some intensity analysis preliminary to this paper used the FD method instead^{30,31}.

2.1 Formulation

In the frequency domain, both FD and PAGE methods find the particle velocity by estimating the spatial gradient of the pressure via Euler's equation:

$$j\omega\rho_0\mathbf{u} = -\nabla p, \quad (1)$$

where j is the unit imaginary number, ω is the angular frequency, ρ_0 is the ambient density, \mathbf{u} is the frequency-dependent (complex) vector particle velocity and ∇p is the gradient of the complex pressure.

In one dimension, with two microphones (A and B), the FD method uses a direct linear fit to calculate the pressure gradient as:

$$(\nabla p)_x \approx \frac{p_B - p_A}{d_{AB}}, \quad (2)$$

where d_{AB} is the distance between the two microphones. The pressure is approximated as the average value across the two microphones. The commonly used method for calculating acoustic vector intensity is based on the imaginary part of the cross spectrum. The single-sided active intensity is calculated as:

$$I_{x,FD}(\omega) = \frac{-1}{\omega\rho_0 d_{AB}} \text{Im}\{G_{AB}(\omega)\}, \quad (3)$$

where G_{AB} is the single-sided, ensemble-averaged cross-spectrum between the two microphones, a function of angular frequency. This method introduces systematic bias^{33,43,44} because the gradient is estimated via linear interpolation between the two complex pressures, resulting in underprediction of the intensity level

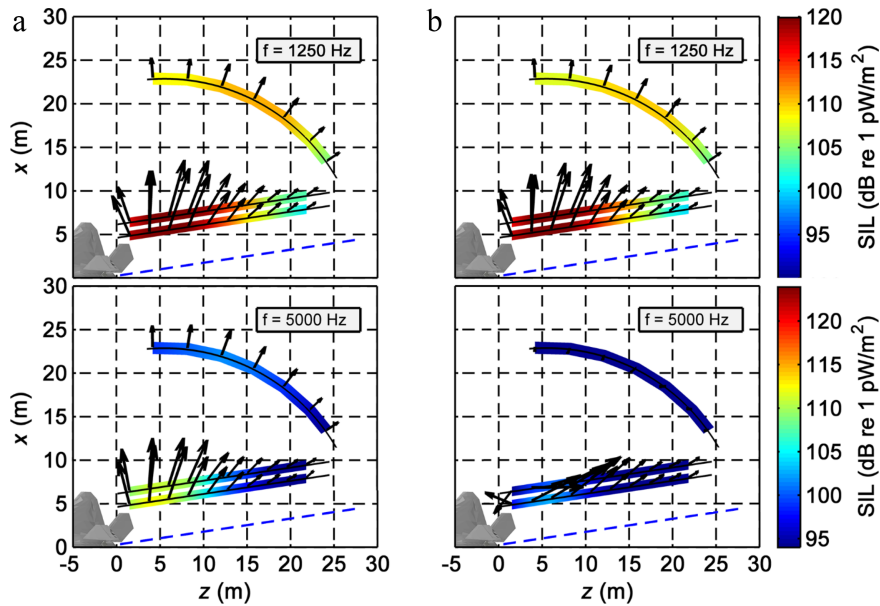


Fig. 5—Acoustic vector intensity maps of the F-22 sound field at 1250 (top) and 5000 Hz (bottom) at afterburner, estimated using the PAGE method (a, left) and the FD method (b, right). The estimated shear layer of the jet exhaust is indicated by a blue dashed line. A rendering of the F-22 is partially visible near the origin, with the engine nozzle shown at the origin. Though both methods agree at 1.25 kHz, for 5 kHz the PAGE method gives physically reasonable intensity directions and magnitudes, while the vector directions predicted by the FD method are clearly nonphysical and the magnitudes are much lower compared to PAGE estimations. For visibility, vector scaling is increased for finite difference at 5 kHz.

at frequencies approaching and well below the spatial Nyquist limit of the two microphones (where the wavelength of the incident pressure wave is twice the separation distance).

The PAGE method instead splits the complex pressure into amplitude and phase components, P and φ , respectively, as $p = Pe^{-j\varphi}$. The gradient of the pressure is found to be⁴⁵:

$$\nabla p = (\nabla P - jP\nabla\varphi)e^{-j\varphi}, \quad (4)$$

and the active intensity is calculated as:

$$\mathbf{I} = \frac{1}{\omega\rho_0} P^2 \nabla\varphi, \quad (5)$$

which in one dimension, with two microphones, is simplified to the expression:

$$\begin{aligned} I_{x, \text{PAGE}} &= \frac{\varphi_B - \varphi_A}{\omega\rho_0 d_{AB}} \left(\frac{|P_A| + |P_B|}{2} \right)^2 \\ &= -\frac{\arg\{H_{AB}\}}{\omega\rho_0 d_{AB}} \left(\frac{|P_A| + |P_B|}{2} \right)^2, \end{aligned} \quad (6)$$

where H_{AB} is the time-averaged transfer function between the two microphones and $|P_A|$ and $|P_B|$ are the

time-averaged complex pressure amplitudes. Because the amplitudes of the complex pressures are averaged instead of using the cross spectrum, the systematic level bias inherent in the FD method is avoided. In addition, the method can be extended beyond the Nyquist limit of the microphone pair by unwrapping the transfer function phase, $\arg\{H_{AB}\}$, in post-processing, thus removing any discontinuous jumps of 2π . Details of this derivation are found in Ref. 33.

The above formulation estimates the active intensity in one dimension, at a point centered between two microphones and collinear with the axis connecting the two microphones. To calculate the intensity in three dimensions using a tetrahedral intensity probe (such as that used in the F-22 measurements), the intensity components between the four microphones must be weighted and summed. Using an extension of the FD method, the three-dimensional intensity can be found by weighting and summing the cross-spectra between the four microphones according to a least-squares method developed by Pascal and Li⁴⁶ and recently implemented by Wiederhold et al.⁴⁷ This process is mathematically equivalent for the PAGE method in three dimensions, except that the transfer function phases are weighted and summed instead of the cross spectra.

2.2 Performance of PAGE vs. FD

In general, acoustic intensity estimates based on averaging the phase and amplitude differences, as in the PAGE method, provide more accurate results over a larger range of frequencies than the FD method. Because of the systematic bias errors inherent in the FD method, at just half the Nyquist frequency, the estimated intensity magnitude error is approximately 2 dB for a plane progressive wave⁴⁴. However, the PAGE method with phase unwrapping removes this upper limit, providing accurate estimates wherever the transfer function, H_{AB} , is well-behaved.

The magnitudes of the F-22 intensity estimates using FD and PAGE methods can be compared to the sound pressure levels as a benchmark for accuracy. In a traveling wave, the sound intensity level (SIL) and sound pressure level (SPL) are by definition approximately equivalent in dB. Above 100 Hz and for the data locations in the F-22 measurement, the intensity is expected to be dominated by the propagating acoustic wave; thus, the SIL and SPL are expected to be approximately equal as a function of frequency. The points at which the estimated SIL and the measured SPL diverge indicate the upper limit of the usable frequency bandwidth for accurate intensity estimation by each method. Figure 6 shows the SIL from the PAGE and FD methods

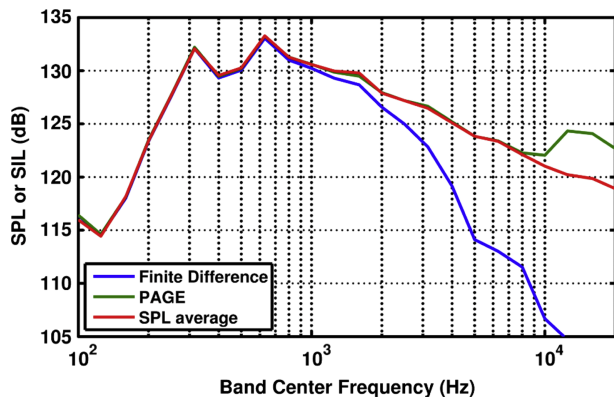


Fig. 6—One-third octave sound pressure levels (SPL) averaged over the four intensity probe microphones, compared with the sound intensity levels (SIL) estimated using the finite difference (FD) and the PAGE method. The FD method underpredicts the intensity level beginning at 1 kHz, while the PAGE method SIL matches the SPL up to about 8 kHz. Below 500 Hz, a relative phase calibration between the four intensity probe microphones has been applied in post-processing.

versus SPL, averaged over the four intensity probe microphones, at one location along measurement plane 2. The FD results begin to diverge starting at about 2 kHz, while the SIL from the PAGE results follow the SPL until about 8 kHz. The spacing between microphones on the intensity probe corresponds to a spatial Nyquist frequency of 5.2 kHz, so this amplitude-based measure of performance largely follows and confirms theoretical prediction. The slight disagreement between SIL from both methods and the measured SPL near 100 Hz is likely due to error in the phase calibrations between the probe microphones. For this figure and all successive results, the SIL is referenced to 1 picowatt per square meter (10^{-12} W/m²).

To directly demonstrate the advantage of the PAGE method over FD, example acoustic vector intensity maps of the F-22 sound field for 1.25 and 5.0 kHz at afterburner are shown in Fig. 5, estimated using both methods. A more complete collection of intensity vector maps using the PAGE method is given in Sec. 3. Both methods provide the same results at 1.25 kHz, well below the spatial Nyquist frequency of the intensity probe. However, at 5 kHz, the vectors given by the FD method are clearly nonphysical and significantly underpredict the intensity magnitudes given by the PAGE method.

3 VECTOR INTENSITY MAPS

Estimated intensity vectors at one-third-octave band center frequencies of 125, 160, 200, 250, 315 and 500 Hz are shown in Fig. 7 at afterburner and in Fig. 8 for military engine conditions. Higher-frequency results at 800 Hz, and 1.25, 2.5 and 5.0 kHz are shown in Figs. 9 and 10. The PAGE method is used for these calculations, so that accurate results above 2 kHz are possible. Only the horizontal (x - z) intensity components are displayed. A rendering of the F-22 is partially visible near the origin, with the engine nozzle centered at the origin. The linear internal scaling used by the rendering program to define vector lengths is kept consistent between the afterburner and military power figures for comparison purposes, but differs between the lower frequency plots (Figs. 7 and 8) and higher frequency plots (Figs. 9 and 10). The lengths of the intensity vectors are cube-root scaled for purposes of illustration and length scaling is also increased at 5 kHz for visibility. The actual sound intensity levels (SIL) are indicated by the color bars and include energy within the 5.9 Hz frequency bin used in the calculation. The data were time-averaged over the full length of each static engine firing, about 25 seconds. As a note, the prior phase calibration performed in the field and used for preliminary studies^{30,31} has been found to be inaccurate. A

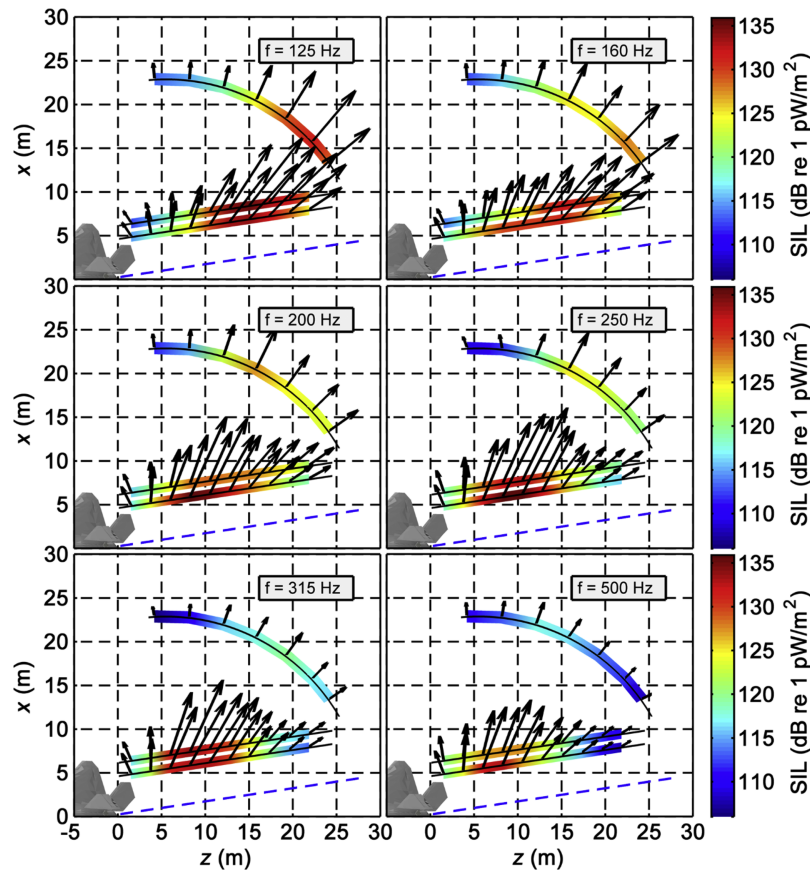


Fig. 7—Acoustic intensity at afterburner engine conditions for select one-third octave band center frequencies. The intensity probe was located at the base of each vector arrow. The estimated shear layer is indicated by a blue dashed line. Vector length scaling used by the rendering program is kept consistent between this figure and Fig. 9. Note how the region of maximum intensity shifts upstream with increasing frequency, while the overall sound intensity level decreases. Maximum intensity magnitude levels are higher at afterburner than at military engine conditions by up to 5 dB.

subsequent, laboratory microphone interchange calibration was performed and has been applied below 500 Hz for the results shown in this paper.

Study of the intensity vector estimates in Figs. 7–10 elucidates the frequency-dependent nature of the F-22 sound field. The region of maximum intensity moves upstream with increasing frequency up to about 800 Hz, above which the location of the maximum intensity region stays fairly consistent, while the overall intensity magnitude decreases as expected from a typical jet noise power spectrum. The largest magnitude intensity vectors are unidirectional at low frequencies. For example, compare the smaller directional variation in the largest intensity vectors at 125 Hz (near $z = 20$ m), to the wider spread of vector directions at 1250 Hz, with maximum intensity near $z = 5$ m. At the higher frequencies, the rapid change in the vector directions as the probe position goes from zero to 10 m downstream suggests an omnidirectional source component close to the nozzle, which becomes more prominent as frequency increases.

Another interesting feature seen at some of the low frequencies is an apparent dual intensity maximum along the measurement plane. In Fig. 8 at 125 Hz, one region of maximum intensity is observed, centered near $z = 18$ m downstream along measurement planes 1 and 2. At 160 Hz, the intensity vectors remain large around $z = 18$ m but another group of intensity vectors rise in magnitude near $z = 8$ m, which point in a different direction than those farther downstream. By 200 Hz, the vectors in the second region ($z = 8$ m) have increased in magnitude over the region farther downstream and continue to increase somewhat at 250 Hz. Similar behavior is observed for afterburner in Fig. 7. This 125–250 Hz band corresponds to the same frequency region over which there is a dual peak in the spectral shapes, as identified by Neilsen et al.³⁹ and further investigated by Tam and Parrish⁴⁸. Acoustical holography results show two prominent lobes of radiation at these frequencies, with low coherence between the lobes, giving further credence to the presence of independent

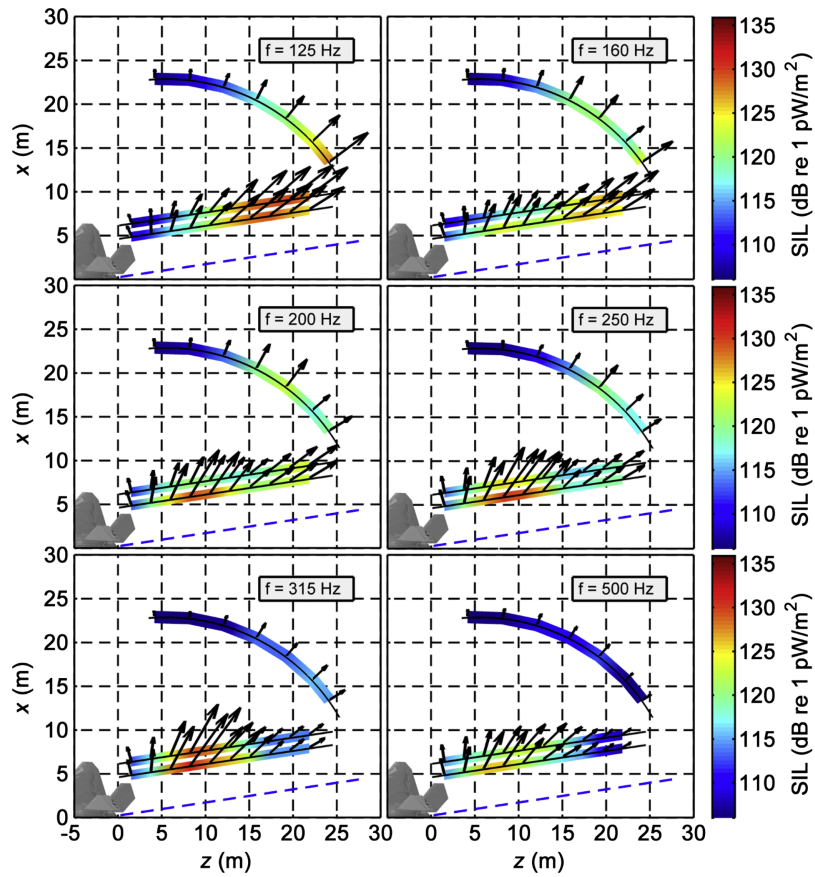


Fig. 8—Similar to Fig. 7 except at military power. Vector scaling is kept consistent between this figure and Fig. 7.

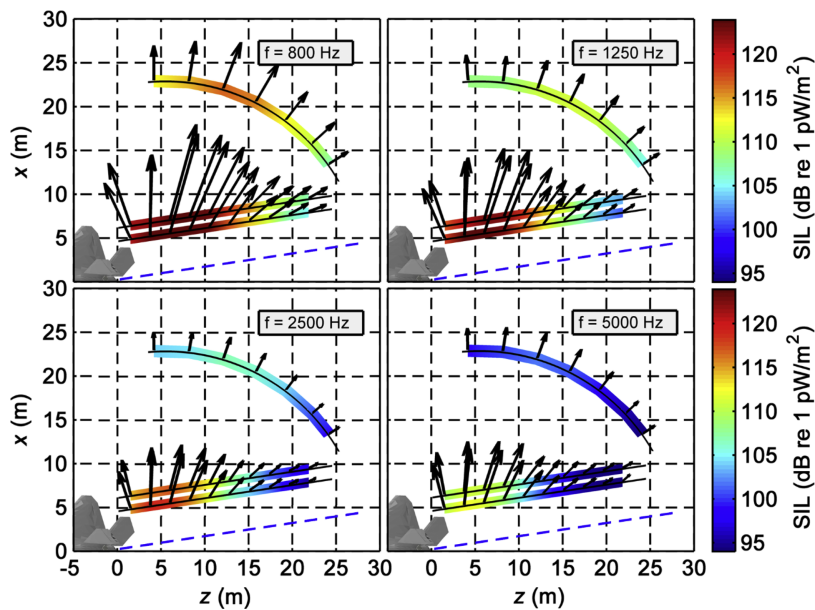


Fig. 9—Acoustic intensity at afterburner engine conditions for select one-third octave band center frequencies. The intensity probe was located at the base of each vector arrow. The estimated shear layer is indicated by a blue dashed line. Vector length scaling used by the rendering program is kept consistent between this figure and Fig. 10, while scaling at 5 kHz is increased for visibility. Note how the maximum intensity region location is generally consistent at these frequencies, while the overall sound intensity level decreases at higher frequencies.

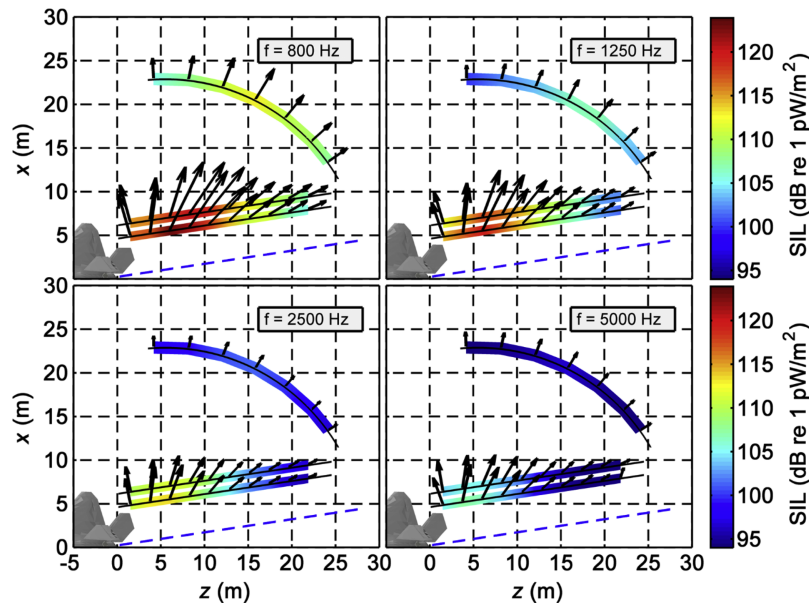


Fig. 10—Similar to Fig. 8 except at military power. Vector scaling is kept consistent between this figure and Fig. 8, while scaling at 5 kHz is increased for visibility. Maximum intensity magnitude levels are lower at military than at afterburner engine conditions by up to 5–7 dB.

source mechanisms³⁶. In addition, an intensity-based equivalent source model using two analytical, mutually incoherent steered line array sources has produced features consistent with these measurements, with greater success than the use of a single steered line array³¹.

Some initial qualitative comparisons between engine conditions can be made from the intensity maps in Figs. 7–10. At all frequencies, the maximum intensity magnitudes at afterburner exceed those at military by up to 5–7 dB and maximum intensity vectors at afterburner can be observed to point slightly farther to the fore. From 125 to 160 Hz, more sound energy is shifted downstream at afterburner than at military. These observations are quantified below in Sec. 4.

Because the probe took data at a height of about 2.54 m above a hard surface consisting of a concrete pad and rain-packed dirt, ground reflections have a noticeable effect on the acoustic vector intensity. At 125 Hz, as seen in Figs. 7 and 8, intensity vectors in the maximum intensity region along measurement plane 2 near $z = 20$ m have magnitudes about 1.5 dB higher than those along plane 1. This is contrary to expectation based on geometric spreading and is due to the interference of direct and reflected signals. For example, the intensity from a monopole at $z = 10$ m along the jet axis, with the same measurement geometry, produces constructive interference resulting in a relative +2 dB magnitude near $z = 20$ m along plane 2. The presence of ground reflection interference is readily observed in planar measurements from the 90-microphone array⁴⁰.

4 ANALYSIS

4.1 Maximum Intensity Directions

The intensity maps shown above clearly illustrate the presence of a spatially extended source, with frequency-dependent characteristics. To better describe the most dominant portion of the sound field, at each frequency, a “3 dB-down” region is defined to include all intensity vectors with magnitudes within 3 dB of the maximum at that frequency. Because of the limited, discrete number of data locations, a linear interpolation between vector intensity magnitudes in dB and vector angles is performed, as shown in Fig. 11. All interpolated intensity vectors within the 3 dB-down mark are included in the region, allowing for a higher-resolution representation and smoother results as a function of frequency. The source characterization in this section is based on analysis of these interpolated 3 dB-down regions along measurement plane 2 only. As noted in Sec. 1.2, systematic error at frequencies below 2 kHz is expected to be <1 dB maximum error in magnitude and <10° direction error⁴¹.

Figure 12 displays the range of angles corresponding to intensity vectors contained within the 3 dB-down regions as a function of frequency. Specifically, the results are shown at one-third octave band center frequencies, but narrowband intensity vectors have been integrated over the one-third octave band. Key features of the sound field that have ties to source features are illustrated here. First, the variability of the vector directions increases with increasing frequency, most notably

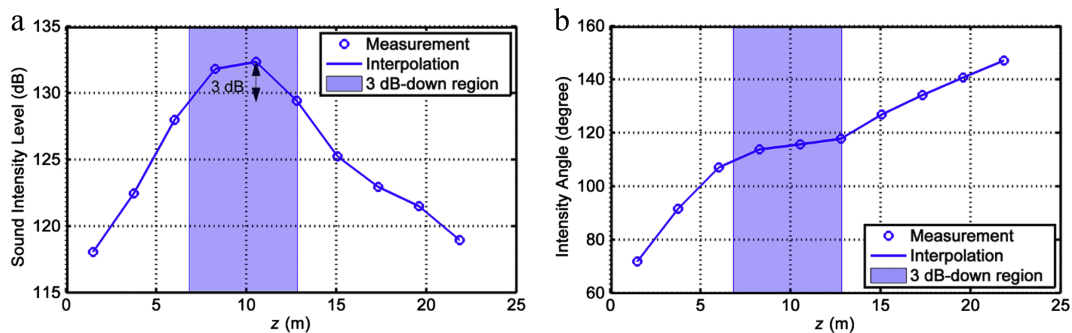


Fig. 11—Example of F-22 acoustic intensity magnitudes (a) and angles measured from the engine inlet (b) as a function of downstream distance along plane 2. Measurement points are shown as circles, connected by the linear interpolation. All interpolated vectors within the shaded blue region are included in the 3-dB-down region analyzed throughout this section.

at frequencies approaching 1 kHz. Below this frequency, the energy flow is much more unidirectional, indicative of the dominance of a directional, low-frequency source. At higher frequencies, a more omnidirectional source appears to rise in prominence. This rather rapid change in directionality at high frequencies is reminiscent of the Tam two-source model⁴⁹, where noise at the sideline is dominated by high-characteristic-frequency, omnidirectional radiators due to fine-scale turbulence, whereas the unidirectional downstream noise is the result of large-scale turbulent structures with lower characteristic frequencies. It is perhaps not coincidental that the 1 kHz frequency transition in behavior is similar to the 1–2 kHz peak frequencies of the fine-scale similarity spectra used by Neilsen et al.³⁹ to match the measured F-22 spectra at the sideline.

Though the general trend is for the maximum intensity vectors to shift forward 10–15° as frequency increases, large variation in their direction is evident before 1 kHz, most notably for military engine conditions. A study of the vector maps in Sec. 3 (Figs. 7 and 8) explains the rapid transition between directions around 200 Hz. As noted above, between about 160 and 250 Hz, two discrete regions of maximum intensity are evident at measurement planes 1 and 2, which shift in prominence. Note how the most pronounced intensity vector directions differ between these two regions; thus, the angles corresponding to vectors that are within 3 dB-down of the maximum one at each frequency, along plane 2, shifts discretely between 160 and 250 Hz. This effect is most notable at military engine conditions; the directions shift from 141 to 145° at 200 Hz to 111–128° in the 250 Hz third-octave band. Comparison with Fig. 8 at 200 and 250 Hz (along measurement plane 2) illustrates directly the shift in prominence between the 3 dB-down region centered around $z = 20$ m downstream, to a region centered around $z = 10$ m, with these differing directionalities.

Comparisons can be drawn between the vector directions in the 3-dB down regions at afterburner and the measured far-field directivity of the F-22. The directivity of the F-22 at afterburner was previously measured with 10° resolution between 115 and 145° at distances of 61 and 305 m⁵⁰. At 100–160 Hz, sound levels from the F-22 were greatest between 125 and 135°, while at or above 200 Hz, a measured directivity of 115° dominated (as the measurements did not extend farther forward). The maximum OASPL directivity angle was 125°⁴⁰. The vector directions in Fig. 12, however, show dominant radiation at 106–138° from 100 to 200 Hz, then 105–120° between 200 and 1000 Hz and even farther forward above 1000 Hz. Thus, the regions of maximum levels above about 200 Hz in geometric near- and mid-field energy flow are likely important in directions farther forward than the maximum far-field directivity angle. The direction of the plane 2 intensity vectors in the 3 dB-down regions aligns somewhat with the maximum directivity angle only for 100–200 Hz.

The most notable difference between the two engine conditions is that the intensity vector angles at afterburner are directed up to 10° farther forward on average than for military engine conditions. For example, at 1 kHz, the vectors at afterburner point at 92–115° relative to the engine inlet, but at 110–128° for military power. The difference is evident across all frequencies. In addition, the vector directions at military are more unidirectional up to about 600 Hz, shifting to a more omnidirectional trend thereafter; interestingly, this shift occurs more smoothly above 600 Hz at afterburner. The difference in the frequency at which the shift to omnidirectionality occurs at afterburner may be explained by further reference to the similarity spectra analysis by Neilsen et al.³⁹, according to the Tam two-source model, as a function of engine condition. To the side of the engine nozzle exit (90°), for military engine conditions, the contributions from both similarity spectra,

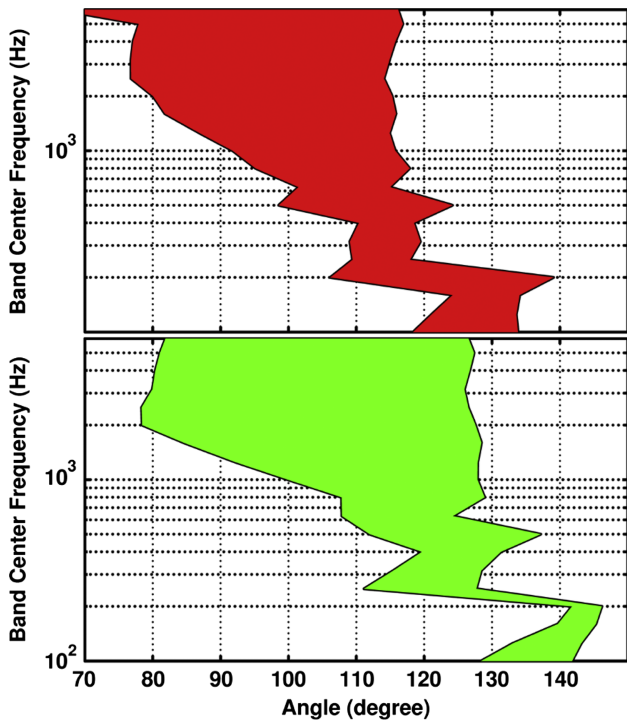


Fig. 12—Angular span of the acoustic intensity vectors contained within the 3-dB-down regions along plane 2 at one-third octave band center frequencies, after intensity vectors are integrated over one-third octave bands, at afterburner (top) and for military engine conditions (bottom). Angles are measured from the engine inlet. For both conditions, the range of vector directions increases in width for frequencies about 1000 Hz for afterburner and 600 Hz for military, indicating the prominence of a more omnidirectional source. The rapid change at 200–250 Hz is an effect of the transition between two maximum intensity locations with discrete directionalities in that frequency range (as shown in Figs. 7 and 9) and is more apparent at military engine conditions. Also, note how angles at afterburner are up to 10° farther forward than for military conditions.

as needed to match the measured spectrum, are approximately equal by about 600–800 Hz, with the more omnidirectional fine-scale structures dominating at higher frequencies. At afterburner, and again at a 90° , a similar mixed spectrum is shown to match the measured

spectrum, but the crossing point of the two similarity spectra occurs instead at 1 kHz. Hence, for directions where a combination of the two similarity spectra is needed to match the measured spectra, frequencies at which the fine-scale contribution exceeds the large-scale correspond to the shifts towards omnidirectionality shown in Fig. 12.

4.2 Ray-Tracing

As a straightforward method to approximate the frequency-dependent source region, interpolated intensity vectors along measurement plane 2, located 5.6 m to the side of the shear layer, are traced back to the jet centerline. This technique is prompted by the methods of Jaeger and Allen²⁰ in studying subsonic jets and has been applied previously to a 12.7 cm-diameter and 1.1 m-diameter rocket motors⁴¹; however, these studies used all intensity measurement locations in their ray-tracing method. In the present work, narrowband intensity calculations are integrated within a given one-third-octave band and a 3 dB-down region is defined from the resultant intensity vectors, representing the dominant energy in that band, as illustrated in Fig. 11. Vectors within the 3 dB-down region are traced backwards, so that the left-most and right-most intercepts along the jet centerline define an approximate equivalent noise source location and indicate the extent of the source. Similar results up to 3 kHz, using intensity calculated with the finite-difference method, have been reported previously at narrowband frequencies only and without the post-processing phase calibration mentioned in Sec. 3³⁰.

The equivalent source reconstruction results from 100 Hz to 6 kHz are shown in Fig. 13. For both military and afterburner conditions, the ray-traced peak source location moves upstream and its extent contracts with increasing frequency. The comparison between the estimated source regions for the two engine powers shows that the source region for afterburner is about 1 m farther downstream than at military power and is somewhat broader by up to 1 m in width above 200 Hz. As expected from comparison with jets of other scales, the extended source region shown in Fig. 13 is more extended spatially than a subsonic, unheated jet²⁰ and more compact than the source region found in a higher-thrust jet plume such as that emanating from a GEM-60 solid rocket motor²⁹. While the engine flow parameters are generally unknown, for purposes of geometric scaling it should be noted that the hydraulic diameter of the F-22 nozzle is approximately 0.6 m.

The frequency-dependent estimated source location trend in Fig. 13 agrees qualitatively with previous studies on laboratory-scale jet noise^{14–16}. Suzuki and

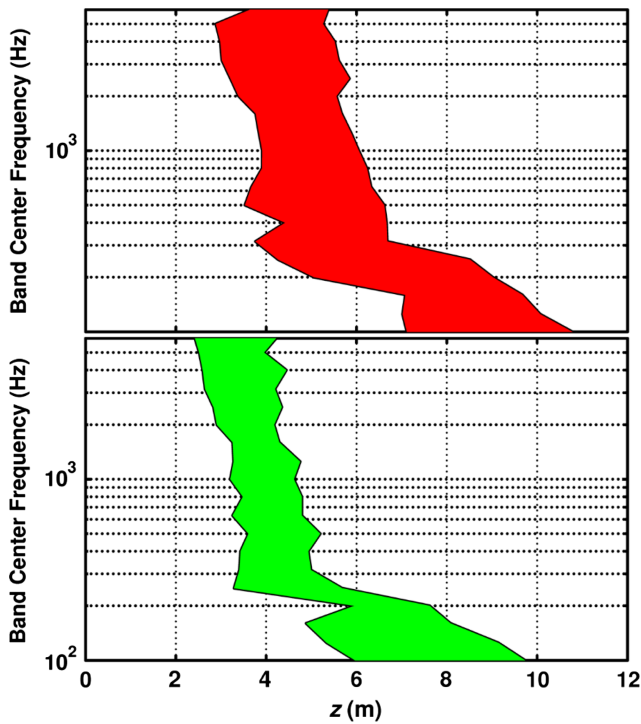


Fig. 13—Generalized equivalent source locations as a function of frequency found from intensity ray-tracing, at afterburner (top) and military engine conditions (bottom). Ray-tracing results are presented at one-third octave band center frequencies, from intensity vectors integrated over each band. The rapid transition region around 200 Hz corresponds to the switch in dominant intensity regions seen in Figs. 7 and 9 and is more apparent at military engine conditions. At all frequencies, resulting source regions at afterburner are about 1 m farther downstream and 1 m wider than for military.

Colonius⁵¹ and Gudmundsson and Colonius⁵² observed from near-field pressure measurements that the source region for a subsonic jet contracts and moves upstream with increasing frequency. However, the observed transition in source location at lower frequencies (from 100 to 250 Hz) for the F-22 occurs more rapidly than similar transition regions in laboratory-scale jets. From a beamforming analysis, Lee and Bridges found that the transition in source location occurred more smoothly over a broader frequency range in a subsonic, heated jet¹⁴. Increasing the acoustic Mach number caused a sharper transition above a Strouhal number (St) of 0.5. However, the frequency range of the

transition was well above the dominant radiation frequencies (from St = 0.1–0.2). By contrast, the transition region in Fig. 13 occurs around the dominant frequencies of the noise from the F-22, about 100–200 Hz in the peak radiation direction.

The significant shift in the locations of the estimated F-22 source region between 100 and 250 Hz, in Fig. 13, corresponds to the discrete change in maximum intensity regions seen in the vector maps in Sec. 3 (Figs. 7 and 8). Recall the presence of the two regions along measurement plane 2 with large intensity vectors that point in different directions. The change in the selection of which one is identified as the maximum 3 dB-down region as frequency increases produces the abrupt change in the ray-tracing results shown in Fig. 13. This effect is most pronounced at military engine conditions, where the estimated source region covering $z = 6\text{--}7.5$ m at 200 Hz shifts upstream to $z = 3.5\text{--}5.5$ at 250 Hz, the next third-octave band. As noted above, the nature of this transition region and the possibility of two discrete source mechanisms are currently being explored^{36,39,48}.

4.3 Ray-Tracing Validation

To better evaluate the physical significance of the resulting ray-traced dominant source regions, a numerical case study has been created in which the simulated intensity vectors calculated from a line of point sources (monopoles), are ray-traced back to the source region, similar to what has been done with the F-22 data. The analytical, axial source distribution chosen for the simulated source incorporates the hyperbolic tangent wavepacket model proposed by Papamoschou⁵³. Two line arrays of closely-spaced monopoles are placed along the jet axis, one at the height of the engine nozzle to simulate the direct source and the other at the same distance below the ground to simulate the ground reflection. The amplitudes of the monopoles were spatially weighted according to the equation:

$$|p(z)| = \tanh \left[\left(\frac{z}{b_1} \right)^{g_1} \right] \left(1 - \tanh \left(\frac{z}{b_2} \right)^{g_2} \right). \quad (7)$$

where b_1, b_2, g_1 and g_2 are input parameters. Two examples of wavepacket-based amplitude distributions are displayed in Fig. 14(b) for 100 Hz and Fig. 15(b) for 250 Hz. This amplitude envelope is then applied to the arrays of monopoles.

Intensity vectors are calculated from two amplitude-shaded line arrays of monopoles, one in which the monopoles are uncorrelated and with a random phase relationship and one in which the monopoles across the entire array are correlated and have a constant phase

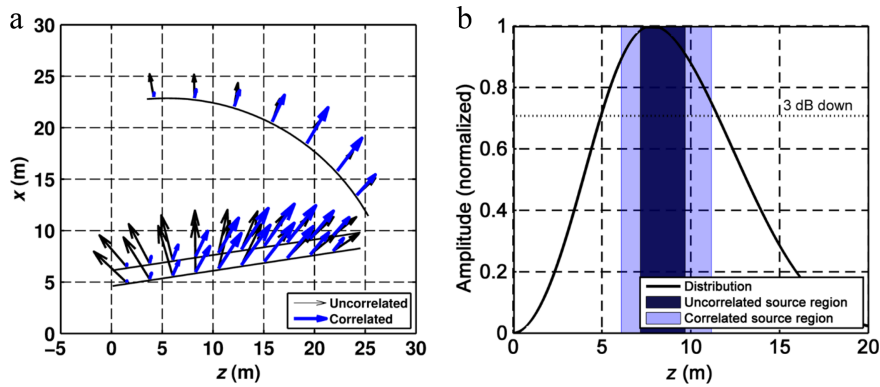


Fig. 14—Simulated intensity fields at 100 Hz (a), resulting from either a correlated or uncorrelated array of amplitude-shaded monopoles and ray-tracing results compared to the actual source distribution, (b). In (a), the black vectors represent the acoustic intensity from an uncorrelated line of point sources with the amplitude distribution shown as the solid line in (b) and random phase relationship. The blue vectors show intensity from a line of point sources with the same distribution and a set phase relationship that produces a correlated source. In (b), the dark blue bar indicates the ray-traced source width from the resultant 3-dB-down region in the uncorrelated case; the light blue indicates the same for the correlated case. A dotted line shows the amplitude that is 3 dB down from the maximum of the source distribution. Note how the ray-tracing method predicts a broader source extent in the correlated case, while approximately the top 1–2 dB of source energy is represented in the source predictions for both source models.

relationship, such that the array is steered towards one physically-relevant direction. The two types of line sources are of interest because of the partially correlated nature of jet noise^{54,55}. Intensity vectors calculated with each line source are shown in Figs. 14(a) and 15(a) for 100 and 250 Hz, respectively, where scaling between the two cases is arbitrary. As with the F-22 data, a 3 dB-down region that includes all linearly interpolated vectors with magnitudes within 3 dB of the maximum for each source type, is defined. The vectors from this region are traced back to the centerline as described in Sec. 4.2. The resulting range of z -intercepts for each source model is shown by shaded regions in Figs. 14(b) and 15(b).

At both frequencies in this numerical case study, the source regions predicted by the ray-tracing include the peak location, but only span about the top 10–20% of the pressure distribution, or the top 1–2 dB of the source energy. The source region width found for the correlated array exceeded that for the uncorrelated array, though the method performs similarly in both cases. Since jet noise sources are expected to exhibit both correlated and uncorrelated characteristics, with the correlated noise dominating at lower frequencies, this performance is encouraging. However, it should be stressed that ray-tracing results from the 3 dB-down regions in the intensity field will not translate directly to the location of the top 3 dB of the source region.

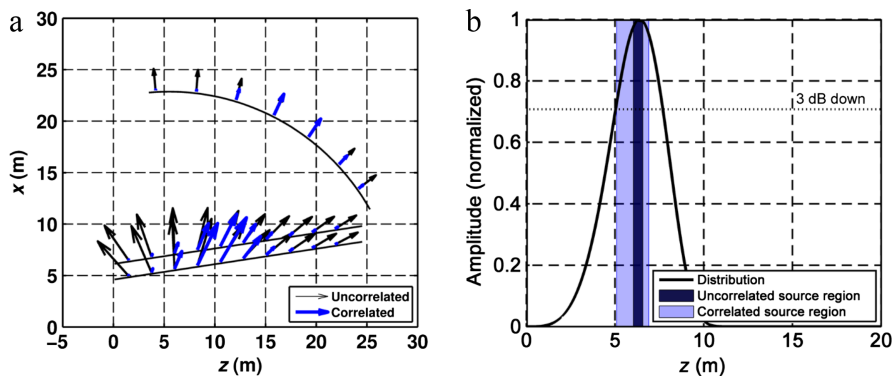


Fig. 15—Similar to Fig. 14 except at 250 Hz.

5 CONCLUSION

A detailed investigation and analysis of the intensity field near an F-22 have led to a characterization of the acoustic sources of turbulent mixing noise from tactical military aircraft. To increase the upper frequency limit of this discussion from less than 3 kHz to about 6 kHz, the novel PAGE method has been used in post-processing of data from a four-microphone intensity probe. Resultant maps of the intensity field at multiple one-third octave band center frequencies and at military and afterburner engine conditions, have been displayed. The region of maximum intensity is shown to move upstream with increasing frequency and around 200 Hz two discrete high-intensity regions with differing intensity directions shift in prominence. The spatial variability in the intensity vector directions is shown to broaden with increasing frequency, as the jet noise sources appear to look more omnidirectional. Maximum intensity vector directions point farther forward by about 10° at afterburner compared to military engine conditions.

A straightforward ray-tracing technique provides an estimate of the peak source location and width, by tracing vectors integrated over one-third octave bands and in 3 dB-down regions back to the jet centerline. The generalized source region is shown to contract and move upstream with increasing frequency, with a transition at low frequencies more rapid than similar transition regions in laboratory-scale jets. The source region at afterburner is consistently about 1 m further downstream and 1 m wider than for military engine conditions. In addition, a numerical case study incorporating an analytical wavepacket model is performed to better interpret the ray-tracing method. Results indicate that the generalized source region predicted by ray tracing from the 3 dB-down regions in the field likely correspond to a region that includes only about the top 1–2 dB of energy at the source. For future work, comparison with results of this same method using intensity data from other scales of supersonic jets and from intensity reconstructions from acoustical holography, will also be beneficial.

6 ACKNOWLEDGMENTS

The authors gratefully acknowledge funding for this analysis from the Office of Naval Research. The measurements were funded by the Air Force Research Laboratory through the SBIR program⁵⁶ and supported through a Cooperative Research and Development Agreement (CRDA) between Blue Ridge Research and Consulting, Brigham Young University and the Air Force. Also, the authors gratefully recognize the efforts of Derek Thomas, Benjamin Christensen and Eric Whiting in the development and implementation of the

PAGE intensity processing method. Distribution A: Approved for public release; distribution unlimited. 88ABW Cleared 07/08/2015; 88ABW-2015-2087.

7 REFERENCES

1. ISO 9614-1:1993, "Acoustics—Determination of sound power levels of noise sources using sound intensity—Part 1: Measurement at discrete points", International Organization for Standardization, (1993).
2. ISO 9614-2:1996, "Acoustics—Determination of sound power levels of noise sources using sound intensity—Part 2: Measurement by scanning", International Organization for Standardization, (1996).
3. ISO 9614-3:2002, "Acoustics—Determination of sound power levels of noise sources using sound intensity—Part 3: Precision method for measurement by scanning", International Organization for Standardization, (2002).
4. ISO 11205:2003, "Acoustics—Noise emitted by machinery and equipment—Engineering method for the determination of emission sound pressure levels in situ at the work station and at other specified positions using sound intensity", International Organization for Standardization, (2003).
5. T. Astrup, "Measurement of sound power using the acoustic intensity method — A consultant's viewpoint", *Appl. Acoust.*, **50**(2), 111–123, (1997).
6. S. Weyna, "The application of sound intensity technique in research on noise abatement in ships", *Appl. Acoust.*, **44**(4), 341–351, (1995).
7. ISO 15186-1:2003, "Acoustics—Measurement of sound insulation in buildings and of building elements using sound intensity—Part 1: Laboratory measurements", International Organization for Standardization, (2003).
8. ISO 15186-2:2010, "Acoustics—Measurement of sound insulation in buildings and of building elements using sound intensity—Part 2: Field measurements", International Organization for Standardization, (2003).
9. Y.S. Wang and M.J. Crocker, "Direct measurement of transmission loss of aircraft structures using the acoustic intensity approach", *Noise Control Engr. J.* **19**(3), 80–85, (1982).
10. X. Qiu, C.H. Hansen and X. Li, "A comparison of near-field acoustic error sensing strategies for the active control of harmonic free field sound radiation", *J. Sound Vibr.*, **215**(1), 81–103, (1998).
11. C. Yu, Z. Zhou and M. Zhuang, "An acoustic intensity-based method for reconstruction of radiated fields", *J. Acoust. Soc. Am.*, **123**(4), 1892–1901, (2008).
12. F. Jacobsen and V. Jaud, "Statistically optimized near field acoustic holography using an array of pressure–velocity probes", *J. Acoust. Soc. Am.*, **121**, 1550–1558, (2007).
13. M.C. Harris, J.D. Blotter and S.D. Sommerfeldt, "Obtaining the complex pressure field at the hologram surface for use in near-field acoustical holography when pressure and in-plane velocities are measured", *J. Acoust. Soc. Am.*, **119**(2), 808–816, (2006).
14. S.S. Lee and J. Bridges, "Phased-array measurements of single flow hot jets", *AIAA Paper 2005–2842*, (2005).
15. D. Papamoschou and A. Dadvar, "Localization of multiple types of jet noise sources", *AIAA Paper 2006–2644*, (2006).
16. R. Dougherty and J. Mendoza, "Phased array beamforming with 100-foot polar arc microphones in a static engine noise test", *AIAA Paper No. 2008–51*, (2008).
17. C.K.W. Tam, K. Viswanathan, N.N. Pastouchenko and B. Tam, "Continuation of the near acoustic field of a jet to the far field. Part II: Experimental validation and noise source characteristics", *AIAA Paper 2010–3729*, (2010).
18. K. Viswanathan, "Instrumentation considerations for accurate jet noise measurements", *AIAA J.*, **44**(6), 1137–1149, (2006).

19. B.J. Greska, "Supersonic jet noise and its reduction using microjet injection", Ph.D. dissertation, Florida State University, (2005).
20. S.M. Jaeger and C.S. Allen, "Two-dimensional sound intensity analysis of jet noise", *AIAA Paper 93-4342*, (1993).
21. S.R. Ventakesh, D.R. Poak and S. Narayana, "Beamforming algorithm for distributed source localization and its application to jet noise", *AIAA J.*, **41**(7), 1238-1246, (2003).
22. J.M. Seiner, L.S. Ukeiley and B.J. Jansen, "Aero-performance efficient noise reduction for the F404-400 engine", *AIAA Paper 2005-3048*, (2005).
23. S. Martens, J.T. Spyropoulos and Z. Nagel, "The effect of chevrons on crackle—Engine and scalemodel results", *ASME Turbo Expo 2011*, Paper No. GT2011-46417, (2011).
24. N.E. Murray and B.J. Jansen, "Performance efficient jet noise reduction for supersonic nozzles", *Int. J. Aeroacoust.*, **11**(7 and 8), 937-956, (2012).
25. R. Schlinker, S. Liljenberg, D. Polak, K. Post, C. Chipman and A. Stern, "Supersonic Jet noise characteristics and propagation: Engine and model scale", *AIAA Paper 2007-3623*, (2007).
26. A.C. Pietrasanta, "Noise measurements around some jet aircraft", *J. Acoust. Soc. Am.*, **28**(3), 434-442, (1956).
27. J.N. Cole and J.F. Rose, "Acoustic environments of the F-111A aircraft during ground runup", *AMRL-TR-68-14*, Aerospace Medical Research Laboratories, U.S. Air Force, Wright-Patterson Air Force Base, (1968).
28. K.L. Gee, J.H. Giraud, J.D. Blotter and S.D. Sommerfeldt, "Near-field vector intensity measurements of a small solid rocket motor", *J. Acoust. Soc. Am.*, **128**(2), EL69-EL74, (2010).
29. K.L. Gee, J.H. Giraud, J.D. Blotter and S.D. Sommerfeldt, "Energy-based acoustical measurements of rocket noise", *AIAA Paper 2009-3165*, (2009).
30. T.A. Stout, K.L. Gee, T.B. Neilsen, A.T. Wall and M.M. James, "Acoustic intensity near a high-powered military jet aircraft", *J. Acoust. Soc. Am.*, **138**(1), EL1-EL7, (2015).
31. T.A. Stout, K.L. Gee, T.B. Neilsen, A.T. Wall and M.M. James, "Intensity analysis of the dominant frequencies of military jet aircraft noise", *Mtgs. Acoust.*, **20**(1), 040010, (2014).
32. S.A. McInerny, "Rocket noise — A review", *AIAA paper 1990-3981*, (1990).
33. D.C. Thomas, B.Y. Christensen and K.L. Gee, "Phase and amplitude gradient method for the estimation of acoustic vector quantities", *J. Acoust. Soc. Am.*, **137**(6), 3366-3376, (2015).
34. A.T. Wall, K.L. Gee, M.M. James, K.A. Bradley, S.A. McInerny and T.B. Neilsen, "Near-field noise measurements of a high-performance jet aircraft", *Noise Control Engr. J.*, **60**(4), 421-434, (2012).
35. A.T. Wall, K.L. Gee, T.B. Neilsen, R.L. McKinley and M.M. James, "Military jet noise source imaging using multi-source statistically optimized near-field acoustical holography", *J. Acoust. Soc. Am.* (submitted 2015)
36. A.T. Wall, K.L. Gee, T.B. Neilsen, B.M. Harker, S.A. McInerny, R.L. McKinley and M.M. James, "Investigation of multi-lobed fighter jet noise sources using acoustical holography and partial field decomposition methods", *AIAA paper 2015-2379*, (2015).
37. B.M. Harker, T.B. Neilsen, K.L. Gee, A.T. Wall and M.M. James, "Spatiotemporal correlation analysis of jet noise from a high-performance military aircraft", *AIAA paper 2015-2376*, (2015).
38. B.M. Harker, K.L. Gee, T.B. Neilsen, A.T. Wall and M.M. James, "Phased-array measurements of full-scale military jet noise", *AIAA Paper 2014-3069*, (2014).
39. T.B. Neilsen, K.L. Gee, A.T. Wall and M.M. James, "Similarity spectra analysis of high-performance jet aircraft noise", *J. Acoust. Soc. Am.*, **133**(4), 2116, (2013).
40. J. Morgan, T.B. Neilsen, K.L. Gee, A.T. Wall and M.M. James, "Simple-source model of high-power jet aircraft noise", *Noise Control Engr. J.* **60**, 435-449, (2012).
41. J.H. Giraud, "Experimental analysis of energy-based acoustic arrays for measurement of rocket noise fields", Masters thesis, Dept. of Physics and Astronomy, Brigham Young University, (2013).
42. R. Raangs, W.F. Druyvesteyn and H.E. De Bree, "A low-cost intensity probe", *Journal of the Audio Engineering Society*, **51**(5), 344-357, (2003).
43. F. Jacobsen, "Sound intensity measurements", in *Handbook of Noise and Vibration Control*, Ed., M.J. Crocker, John Wiley, Hoboken, NJ, (2007), 534-548.
44. F.J. Fahy, *Sound Intensity*, CRC Press, 97-105, (2002).
45. J.A. Mann, J. Tichy and A.J. Romano, "Instantaneous and time-averaged energy transfer in acoustic fields", *J. Acoust. Soc. Am.*, **82**(1), 17-30, (1987).
46. J.-C. Pascal and J.-F. Li, "A systematic method to obtain 3D finite-difference formulations for acoustic intensity and other energy quantities", *J. Sound Vibr.*, **310**(4), 1093-1111, (2008).
47. C.P. Wiederhold, K.L. Gee, J.D. Blotter, S.D. Sommerfeldt and J.H. Giraud, "Comparison of multimicrophone probe design and processing methods in measuring acoustic intensity", *J. Acoust. Soc. Am.*, **135**(5), 2797-2807, (2014).
48. C.K.W. Tam and S.A. Parrish, "Noise of high-performance aircraft at afterburner", *J. Sound and Vibr.*, **352**, 103-128, (2015).
49. C.K.W. Tam, M. Golebiowski and J.M. Seiner, "On the two components of turbulent mixing noise from supersonic jets", *AIAA Paper 96-1716*, (1996).
50. K.L. Gee, V.W. Sparrow, M.M. James, J.M. Downing, C.M. Hobbs, T.B. Gabrielson and A.A. Atchley, "The role of nonlinear effects in the propagation of noise from high-power jet aircraft", *J. Acoust. Soc. Am.*, **123**(6), 4082-4093, (2008).
51. T. Suzuki and T. Colonius, "Instability waves in a subsonic round jet detected using a near-field phased microphone array", *J. Fluid Mech.*, **565**, 197-226, (2006).
52. K. Gudmundsson and T. Colonius, "Instability wave models for the near-field fluctuations of turbulent jets", *J. Fluid Mech.*, **689**, 97-128, (2011).
53. D. Papamoschou, "Wavepacket modeling of the jet noise source", *AIAA Paper 2011-2835*, (2011).
54. C.K.W. Tam, K. Viswanathan, K.K. Ahuja and J. Panda, "The sources of jet noise: Experimental evidence", *J. Fluid Mech.*, **615**, 253-292, (2008).
55. K. Viswanathan, J.R. Underbrink and L. Brusniak, "Space-time correlation measurements in near fields of jets", *AIAA J.* **49**(8), 1577-1599, (2011).
56. SBIR DATA RIGHTS—(DFARS 252.227-7018 (JUNE 1995)); Contract Number: FA8650-08-C-6843; Contractor Name and Address: Blue Ridge Research and Consulting, LLC, 29 N Market St, Suite 700, Asheville NC; Expiration of SBIR Data Rights Period: March 17, 2016 (Subject to SBA SBIR Directive of September 24, 2002).